Hot Processing Maps and Microstructural Characteristics of A357 Alloy

Fuwei Kang, Shijie Wei, Jimin Zhang, Enhao Wang, Dezhi Fan, and Shanshan Wang

In this paper, the hot deformation behavior of A357 alloy was investigated by hot compression tests. Isothermal hot compression simulation tests for A357 alloy were carried out at the conditions of deformation temperature of 350-470 °C, strain rate of 0.001-10 s^{-1} and engineering strain of 50%. Based on the Prasad instability criterion and dynamic material model, the hot processing maps of A357 alloy were constructed. The microstructure of compressed samples at different areas of the hot processing map was characterized by metallographic and scanning electron microscope and transmission electron microscope. The experimental results showed that the unstable processing zone of A357 alloy was mainly distributed in the high strain rate (10 s^{-1}) and low-temperature (350, 380 °C) region. With an increase in the strain, the unstable zone expanded from low temperature to high temperature (470 °C). The ideal deformation conditions were deformation temperatures of 380-410 °C and strain rates of 0.001-0.01 s^{-1}, and deformation temperatures of 440-470 °C and strain rates of 0.01-1 s^{-1}. When the A357 alloy was extruded with the optimal hot processing parameters, the results suggested that hot extrusion could make the microstructure uniform and fine, thereby improving mechanical properties, especially when the elongation was up to 19.5% higher than the as-cast A357 alloy.

1. Introduction

As an age-hardened aluminum alloy, A357 alloy is widely used in aviation, aerospace and automotive industries because of its excellent castability, weldability and hot-cracking resistance (Ref. 1, 2). However, coarse eutectic Si particles and AlFeSi-based intermetallic phases in the casting process may limit the application of the alloy. These problems inherent in the casting process can be improved by degas, degeneration treatment and hot working, which bring about a significant microstructural modification of this alloy in size, morphology and distribution of Si particles as well as the intermetallic compounds (Ref. 3-6). Among the preceding techniques, hot working was one of the long-established and important production methods.

Appropriate selection of hot working parameters critically affects the microstructure and properties of the productions or components, and hot processing maps are an effective way to solve this problem (see 3.2 part). For A357 alloy, it is interesting to investigate its hot deformation characteristics, and the extensive works are carried out on casting technique, heat treatment, microstructure and mechanical properties aspects (Ref. 7-12).

Fuwei Kang, Shijie Wei, Jimin Zhang, Enhao Wang, Dezhi Fan, and Shanshan Wang, School of Materials Science and Engineering, Harbin University of Science and Technology, Harbin 150040, China. Contact e-mail: enhaowang@hrbeu.edu.cn.

In fact, the research on the hot deformation behavior and hot working diagram of deformed aluminum alloy has been improved since the deformation strengthening theory developed. For instance, Chen et al. studied the hot deformation behavior of a high Ti 6061 aluminum alloy, implying the processing window is 400-440 °C and 0.001-01 s^{-1} (Ref. 13). Peng et al. studied the hot deformation behavior of the homogenized Al-3.2 Mg-0.4Er aluminum alloy which was investigated at 573-723 K under strain rates of 0.001-1 s^{-1}, and the results showed that the optimum processing conditions are 573 K, 0.001 s^{-1} and 723 K, 0.001-0.1 s^{-1} (Ref. 14).

Studies with respect to the role and mechanism of plastic deformation in improving the performance of cast aluminum alloys have gradually attracted attention. In Wang's work, the plastic deformation behavior of aluminum casting alloys A356/357 showing that at low plastic strains, the matrix strength and eutectic article aspect ratio dominate the work hardening (Ref. 15). Yang et al. studied hot compressive deformation behavior of the as-quenched A357 aluminum alloy, and M. Haghshenas et al. investigated the effect of deformation-heat treatment cycle on the eutectic morphology and mechanical properties of a Thixocast A356 alloy, and their results showed that the flow stress decreases with the decrease in strain rate and the increase in temperature (Ref. 16, 17). Although they have studied the hot deformation of the alloy, the hot deformation softening mechanism and the application of hot processing map to guide the hot deformation need further research.

This paper aims to establish a hot processing map, optimize the hot processing parameters and study the effect of hot deformation on the microstructure and properties of A357 alloy. The flow soft and hot deformation mechanisms for domains were illustrated in the context of microstructural evolution during the process of deformation. Under the guidance of the optimum hot processing parameters, hot extrusion of the A357 alloy will be carried out.

2. Experimental Procedures

The nominal chemical composition of A357 alloy of this study is as follows (all in wt.%): 6.25 Si, 0.7 Mg, 0.18 Ti, Cu 0.15, 0.08 Zn, 0.07 Be and the remainder Al. A number of cylindrical specimens of Φ8 × 12 mm were cut from the cast A357 alloy samples by electrical discharge machining (EDM) and subjected to hot compression experiments using a Gleeble-1500 D hot simulator. The experimental deformation temperatures were determined as 350, 380, 410, 440, 470 °C, and the strain rates were 0.001, 0.01, 0.1, 1 and 10 s^{-1} with the deformation amount of 50%. Specimens were heated with a heating rate of 10 °C/min from room temperature to test temperatures. All the specimens were soaked at the test temperatures for 120 s before compression tests and then deformed to half of their height, namely 50% engineering strain. Hot extrusion was carried out using a 300 t extruder to obtain an extruded rod. After that, the specimens were polished and etched with Keller's reagent for metallographic observation. Microstructural observation before and after deformation was carried out by using scanning electron microscope (SEM, Philips FEI Sirion 200), transmission electron microscope

(TEM, JEM-2100) and optical microscope (OM, Olympus-BX41M). Tensile test was carried out by Instron 5500R universal tensile testing machine.

3. Experimental Results and Discussion

3.1 True Stress–True Strain Curve of the Alloy

Figure 1 shows the true stress–strain curve of hot compression deformation of A357 alloy under different experimental conditions. Deformation temperature and strain rate determine the flow stress value. When the initial strain increases, the flow stress increases rapidly. After the temperature rises, flow stress decreases at the same strain rate and increases with the increase in the strain rate. When the flow stress reaches a maximum value that remains constant or decreases slightly, the balance between work hardening and dynamic softening tends to stabilize the flow stress. Increasing the temperature causes the heat activation to become severe, and the flow stress is significantly lowered at higher deformation temperatures. At
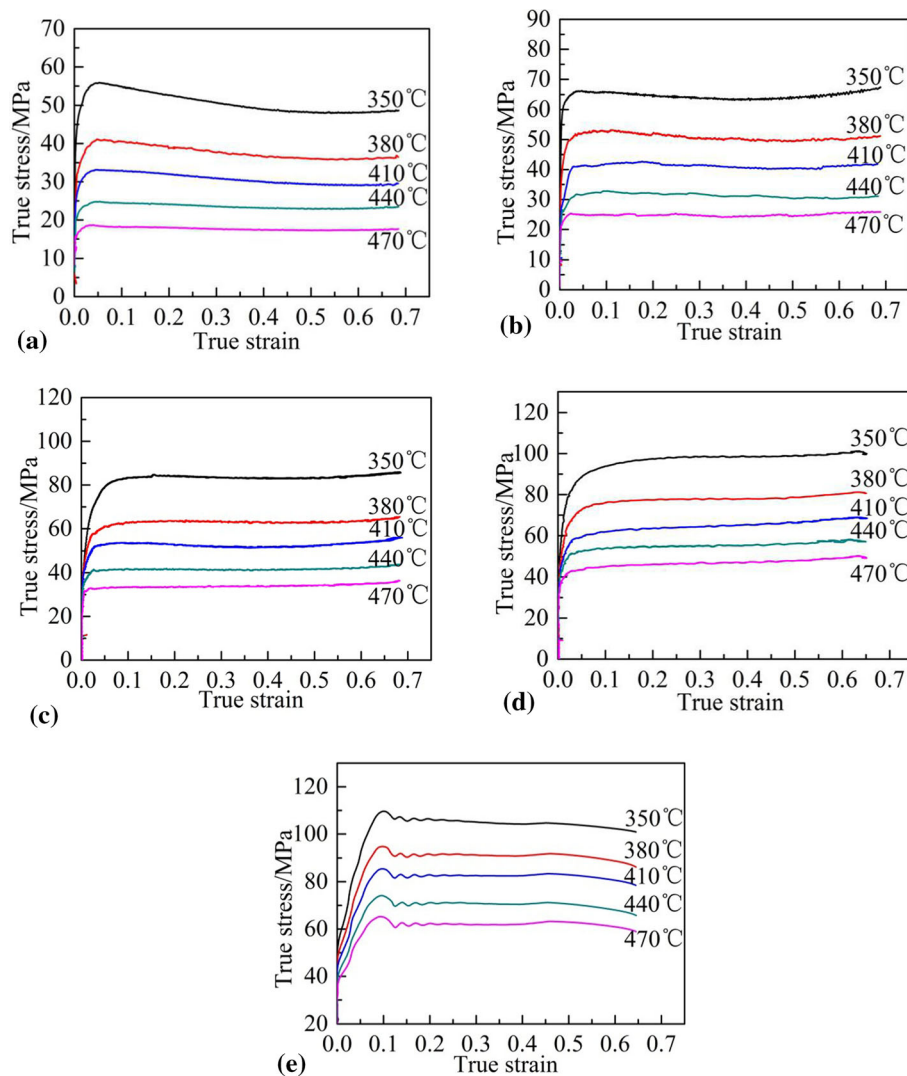

Fig. 1 True stress–strain curves of A357 alloy under compression conditions: (a) 0.001 s^{-1}; (b) 0.01 s^{-1}; (c) 0.1 s^{-1}; (d) 1 s^{-1}; (e) 10 s^{-1}

the same time, the rapid rise in dislocations at higher strain rates causes stress multiplication (Ref. 18, 19).

3.2 Dynamic Materials Model Theory

Hot processing patterns based on dynamic material mode (DMM) are key methods for studying hot processing parameters (Ref. 20, 21). This method has been described previously and has been applied to various materials (Ref. 21-27). The workpiece under hot working conditions can be regarded as a power nonlinear dissipator. The total power consumption P is composed of two complementary parts G and J. The G content represents the power consumption caused by plastic deformation, and the J common content represents the metallurgy. The changes dissipated. The total power consumption P is given by the following equation (Ref. 20):

$$P = \sigma\dot{\varepsilon} = G + J = \int_0^{\dot{\varepsilon}} \sigma d\dot{\varepsilon} + \int_0^{\sigma} \dot{\varepsilon} d\sigma \qquad \text{(Eq 1)}$$

The strain rate sensitivity m is used to partition the power into G content and J co-content by the constitutive flow behavior of the material, and m can be given by the following equation:

$$m = \frac{\partial J}{\partial G}\bigg|_{\dot{\varepsilon},T} = \frac{\partial \ln \sigma}{\partial \ln \dot{\varepsilon}}\bigg|_{\dot{\varepsilon},T} \qquad \text{(Eq 2)}$$

$$\eta = \frac{J}{J_{max}} = \frac{2m}{m+1} \qquad \text{(Eq 3)}$$

A continuum criterion based on the extremism principles of irreversible thermodynamic for the occurrence of flow instabilities can be determined by the following equation (Ref. 28):

$$\xi(\dot{\varepsilon}) = \frac{\partial \ln\left(\frac{m}{m+1}\right)}{\partial \ln \dot{\varepsilon}} + m < 0 \qquad \text{(Eq 4)}$$

where ξ is the instability parameter, which varies with the strain rate and deformation temperature. At the same time, the power dissipation map and the instability map can be obtained. A processing map can be obtained by superimposing an instability map over a power dissipation map (Ref. 28). Dynamic recovery and DRX are main mechanism of flow softening to keep flow stresses and rates of work hardening considerably low. Although these maps give the general guidelines, the interpretation of domains in the map will have to be microstructurally validated (Ref. 29, 30).

3.3 Hot Processing Maps of A357 Alloy

The hot processing map was established at the true stain of 0.4-0.6 following the method in 3.2 section. Figure 2 shows the peak stress and strain rate fitting curves obtained at various deformation conditions. According to Fig. 2, the relationship between peak stress and strain rate can be expressed by the following cubic polynomial (Ref. 5):

$$\ln \sigma = a + b \ln \dot{\varepsilon} + c(\ln \dot{\varepsilon})^2 + d(\ln \dot{\varepsilon})^3 \qquad \text{(Eq 5)}$$

The values of the fitting formula a, b, c and d are shown in Table 1. The m values can be determined by fitting data in Table 1 according to the following equation derived from
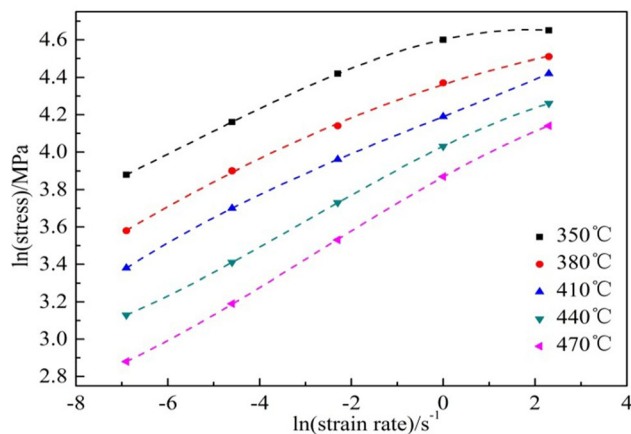

Fig. 2 Polynomial fitting curves from values of peak stress and strain rate at true strain of 0.5

Table 1 Coefficients of a, b, c, and d in polynomial fitting Eq 6

T/°C	Coefficient			
	a	b	c	d
350	4.6	0.054	− 0.012	− 0.00075
380	4.36	0.078	− 0.006	− 0.00007
410	4.19	0.098	− 0.007	0.0004
440	4.03	0.12	− 0.007	− 0.0008
470	3.87	0.14	− 0.006	− 0.0007

Table 2 Values of strain rate sensitivity index m at various deformation conditions

εT/°C	Strain rate/s⁻¹				
	0.001	0.01	0.1	1	10
			m		
350	0.11	0.12	0.10	0.05	0.01
380	0.14	0.12	0.10	0.08	0.05
410	0.16	0.12	0.10	0.10	0.10
440	0.10	0.13	0.14	0.12	0.08
470	0.12	0.15	0.16	0.14	0.1

Equations (Ref. 5) and (2). The calculated results of m values are shown in Table 2.

$$m = \frac{\partial \ln \sigma}{\partial \ln \dot{\varepsilon}} = b \ln \dot{\varepsilon} + 2c(\ln \dot{\varepsilon}) + 3d(\ln \dot{\varepsilon})^2 \qquad \text{(Eq 6)}$$

The values of power dissipation rate η and the instability criterion ξ are calculated based on Eq 3 and 4, as shown in Table 3. Figure 3 and 4 shows the two-dimensional and three-dimensional power dissipation maps, and processing instability maps were established, respectively.

The power dissipation map and the processing instability map were superimposed on each other to obtain the hot

Table 3   Values of η and ξ of A357 alloy under different deformation conditions at true strain of 0.5

$T/°C$ $\dot{\varepsilon}/s^{-1}$	350		380		410		440		470	
	η	ξ	η	ξ	η	ξ	η	ξ	η	ξ
0.001	0.2	0.17	0.25	0.09	0.28	0.07	0.18	0.28	0.21	0.24
0.01	0.21	0.1	0.21	0.05	0.21	0.04	0.23	0.11	0.26	0.19
0.1	0.18	− 0.02	0.18	0.01	0.18	0.05	0.25	0.09	0.28	0.15
1	0.1	− 0.37	0.15	− 0.05	0.18	0.1	0.21	0.02	0.25	0.07
10	0.03	− 2.6	0.1	− 0.18	0.18	0.15	0.15	− 0.21	0.18	− 0.09
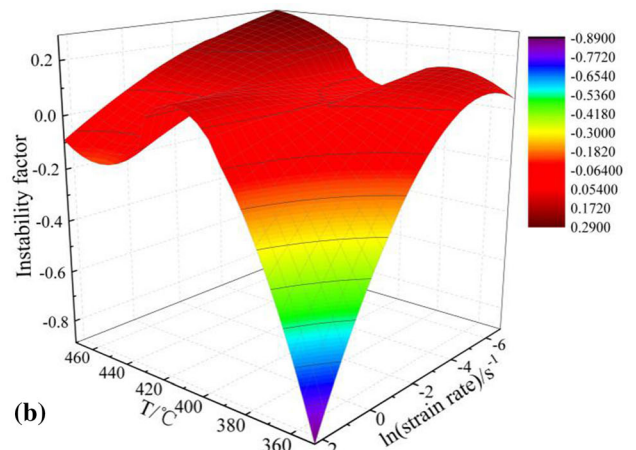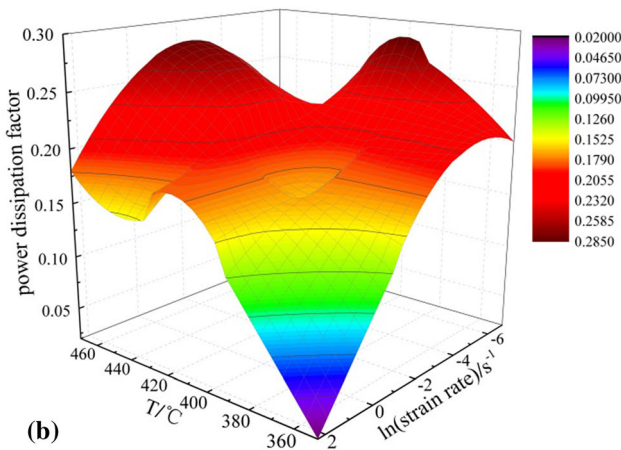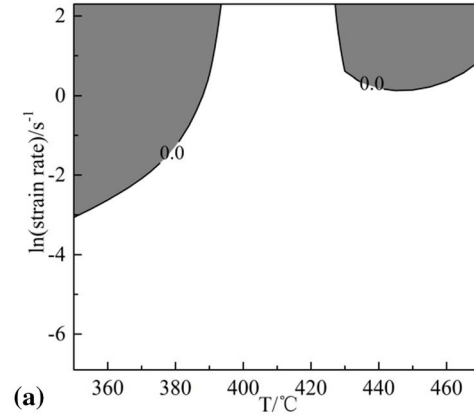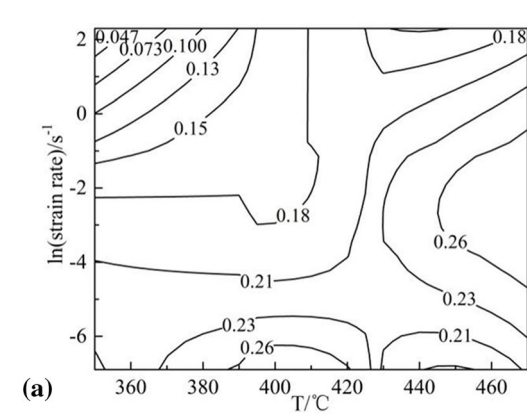
Fig. 3 Power dissipation map for A357 alloy at true strain of 0.5: (a) two dimension; (b) three dimension

Fig. 4 Processing instability map for A357 alloy at true strain of 0.5: (a) two dimension; (b) three dimension

processing map, as shown in Fig. 5. The contours represent the efficiency of power dissipation, and the shaded domains indicate the regions of flow instability.

In the same way, the hot processing maps of A357 alloy also were obtained at true strain of 0.4 and 0.6, respectively, as shown in Fig. 6. It is obvious that the strain value has a significant effect on the processing maps. With the increase in the strain, the instability region expands to the high strain rate and high-temperature region.

During hot deformation, material instability occurs in areas where enthalpy is negative based on instability criteria. As shown in Fig. 5 and 6, unstable regions occur when the strain rate exceeds 0.1 s^{-1}. There is a big difference between the strain of 0.5 in the machining diagram and the unstable region

of the other two strains. As shown in Fig. 5, two unstable regions with a strain of 0.5 appear. The peak efficiency of the region I is about 16 pct, the temperature range is 350-380 °C, and the strain rate ranges from 0.01 to 10 s^{-1}. The peak efficiency of the region II is about 21 pct, the temperature range is 440-470 °C, and the strain rate ranges from 1 to 10 s^{-1}. The rest are safe hot processing regions, but the values of power dissipation rate are not the same in different regions. The ideal hot processing stability regions are region III (380-410 °C, 0.001-0.01 s^{-1}) and region IV (440-470 °C, 0.01-1 s^{-1}), in which the peak efficiency is about 24-26 pct.

Voids, cracks, adiabatic shear bands and other defects are likely to be induced when hot deformation occurs under the
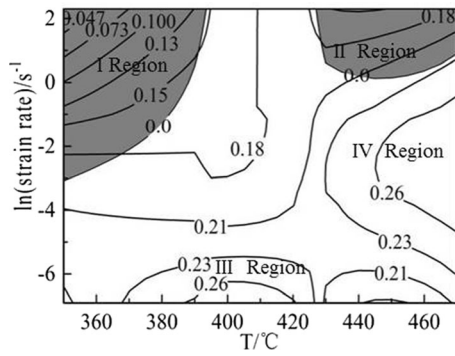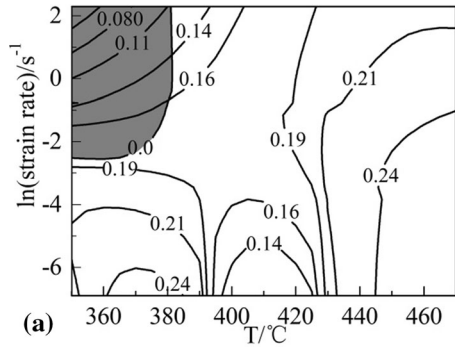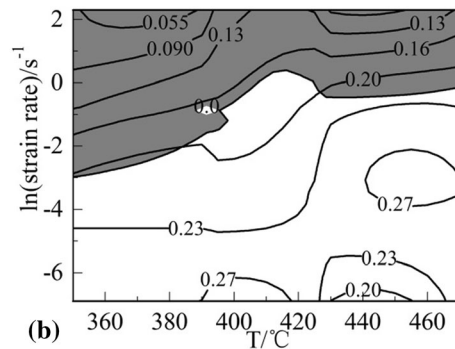
Fig. 5 Hot processing map for A357 alloy obtained at the true strain of 0.5

Fig. 6 Hot processing maps for A357 alloy obtained at different true strain: (a) strain 0.4; (b) strain 0.6

Fig. 7 Optical micrographs of A357 alloy in the instability regions at the true strain of 0.5: (a) region I; (b) region II

Fig. 8 Optical micrographs of A357 alloy in stable regions at true strain of 0.5: (a) region III; (b) region IV

processing parameters corresponding to the flow instability region of metals and alloys, which are disadvantageous to the overall microstructure of the material and the properties of the materials. Therefore, it is necessary to avoid these areas during the hot working process (Ref. 31, 32). As shown in Figs. 4 and 5, processing instability region of A357 alloy was found at high strain rate, and with the increase in strain, the instability region became larger and expanded to high-temperature region. This indicates that the strain and strain rate are the main influencing factors for the hot processing of A357 alloy, and the alloy had a good thermal processing performance at low strain rates.

In the instability regions I and II, as shown in Fig. 5, power dissipation rate decreased rapidly, which may be caused by stress concentration of the deformation, leading to voids, cracks and non-uniform deformation phenomena. The microstructure micrographs of the two regions are shown in Fig. 7. It can be
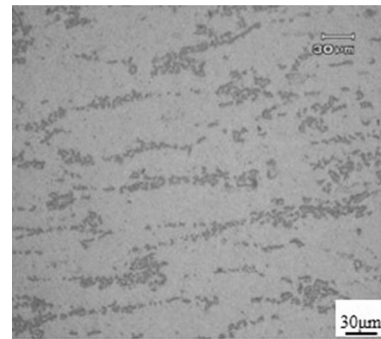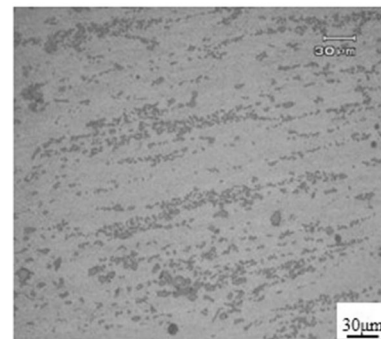
Fig. 9 Morphologies of extruded specimens: (a) at stability region; (b) at instability region

seen that the elongated α-Al phases and the big block and sharp-angled primary silicon are observed obviously in the alloy as marked by arrows in Fig. 7, which shows typical non-uniformly distribution characteristics. In the A357 alloy, the hot workability largely depended on the size, shape and distribution of the primary silicon. The big and sharp-angled silicon phase can severe the matrix and produce stress concentration at the sharp corners, seriously affecting the material properties. It is demonstrated clearly that the extrusions at I and II regions are probably not suitable for this alloy.

Figure 8 presents the microstructures of regions III and IV in Fig. 5. Compared with the microstructure in the instability region in Fig. 6, the eutectic silicon is fine and is of near spherical shape, and the distribution in the matrix is relatively uniform, which can significantly improve hot workability of casting alloy. Therefore, by the analysis of the hot working map and observation of the microstructure, the reasonable hot processing parameters for A357 alloy are obtained, i.e., deformation temperature of 370 °C, strain rate of 0.001 s^{-1}, deformation temperature of 440 °C and strain rate of 1.0 s^{-1}.
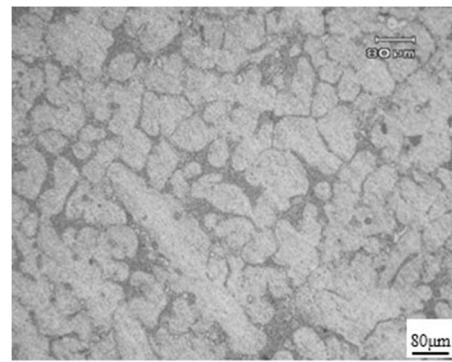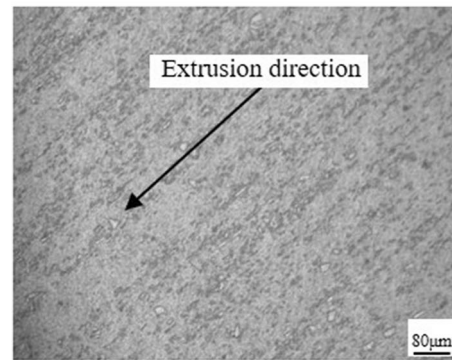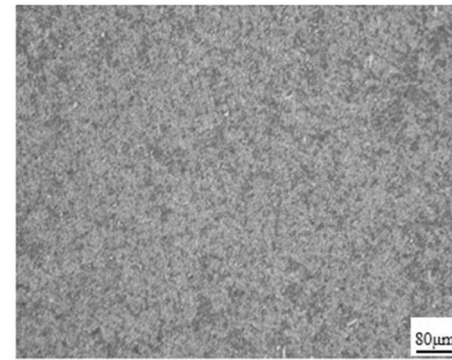

Fig. 10 Microstructures of A357 alloy before and after hot extrusion: (a) before extrusion (as-casting); (b) after extrusion (longitudinal section); (c) after extrusion (transverse section)

4. Extrusion Processing of A357 Alloy

4.1 Macroscopic Morphology of Extruded Specimens

According to the hot processing map, the hot extrusion was conducted at the stability regions and the instability regions, respectively. The extrusion parameters are temperature of 440 °C, ram velocity of 2 mm/s at the stability region, or temperature of 470 °C, ram velocity of 10 mm/s at the instability region. Figure 9 shows the morphologies of extrusions at the stability and instability regions. The surface of stability extrusion bar is smooth, and there are no defects such as peeling, cracks, bubbles and scratches, as shown in Fig. 9(a). The surface of the unstable extruded rod has a wide transverse and longitudinal crack, called fir-tree cracking; this is because
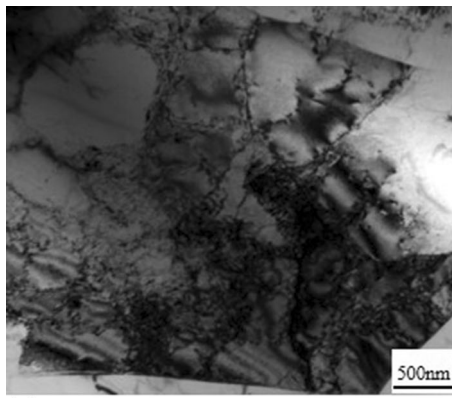
(a)
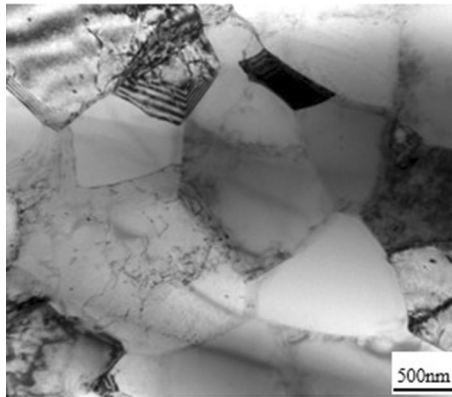
(b)

**Fig. 11** TEM micrographs of samples tested in 350°C at: (a) 0.001 s^{-1}; (b) 10.0 s^{-1}

Table 4 Mechanical properties of A357 alloy in casting and extrusion state

| Alloy state	R_{m}/MPa	A/%
As-casting	174	2.5
As-extruded	208	19.5

the higher strain rate or longitudinal tensile stress exceeds the tensile ultimate strength of its surface.

4.2 Microstructure of as-Extruded Specimens

Figure 10 shows the microstructures of A357 alloy before and after extrusion (*i.e.,* as-casting and as-extruded) in stability region. The microstructure of the A357 alloy before extrusion is shown in Fig. 10(a), which consists of coarse primary silicon particles, continuous α-Al phase and eutectic silicon phase. The microstructures of the A357 alloy after extrusion are shown in Fig. 10(b) and (c) which correspond to micrographs obtained from the longitudinal section and transverse section of the extruded rods, respectively. In Fig. 10(b), it is evident that the parent grains, primary and eutectic silicon phase with 100-300 μm in length and 40-80 μm in width elongated and broke toward the extrusion direction. Microscopic examination, conducted on transverse section of the extruded rod, shows this region is composed of continuous α phase and finely dispersed silicon particles, as shown in Fig. 10(c).
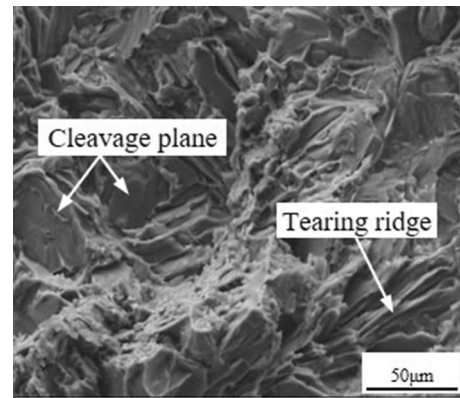
(a)
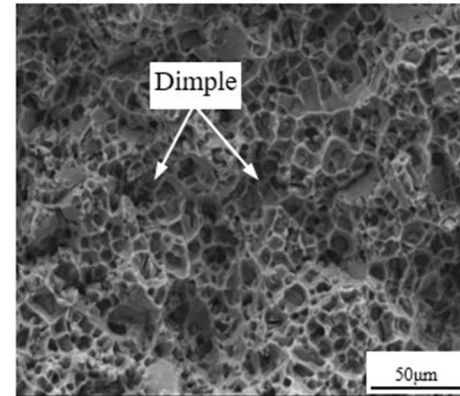
(b)

Fig. 12 SEM micrographs showing the fractographs of before and after extrusion A357 alloy: (a) before extrusion; (b) after extrusion

As is known to all, dynamic recrystallization (DRX) occurs in low stacking fault energy (SFE) metals during hot deformation. In the study of Prasad and Seshacharyulu (Ref. 33), they held the view that DRX did not occur in aluminum due to its high SFE, and the main softening mechanism was only dynamic recovery (DRV) except for high pure aluminum and some alloys containing particle. In other studies, it was highly probable that DRX occurred by adding a large amount of hard particle to form high-density dislocation (Ref. 34-37).

Figure 11 shows the TEM morphologies of A357 samples in 350 °C at the strain rates of 0.001 and 10 s^{-1}. As shown in Fig. 11(a), at the strain rate of 0.001 s^{-1}, a multitude of dislocation tangles were present in the grains and grain boundaries. These boundaries with certain thickness show typical dislocation cell structure, which indicates that the main soften mechanism of this alloy is DRV during this deformation. However, at the strain rates of 10 s^{-1}, DRX occurs in the alloy after thermal deformation, and typical dynamically recrystallized grain formed in parts of the alloy, leading to the decline in dislocation density partly, as shown in Fig. 11(b).

4.3 Mechanical Properties of A357 Alloy Before and After Hot Extrusion

The as-cast and as-extruded A357 alloys were subjected to room-temperature tensile test, and the mechanical properties of the test results are shown in Table 4. The mechanical properties of as-extruded A357 alloy are improved obviously, especially the elongation which increases from 2.5 to 19.5%, whereas the

tensile strength is elevated from 174 MPa to 208 MPa compared to the as-cast condition. It can be seen that from the microstructure of as-extruded alloy, hot extrusion eliminated defects such as porosity in the as-cast microstructure of A357 alloy, refined the silicon phase and increased the homogeneity of the microstructure.

Figure 12 shows the fracture characteristics of A357 alloy before and after extrusion. Many tearing ridges and cleavage planes were observed at the fractured surface of as-cast A357 alloy, as marked by arrows in Fig. 12(a). The fracture mode of the as-cast A357 alloy is a mixed partial brittle fracture mechanism, leading to poor comprehensive mechanical properties. Many equiaxed dimples appeared at the fractured surface of as-extruded A357 alloy, and the dimples evenly distributed in the fractures as marked by arrows in Fig. 12(b). At the same time, elongation was also improved during the tensile process. The results show that the fracture mode of the extruded A357 alloy is mainly ductile fracture (dimple fracture). By comparing both kinds of fracture morphology of this alloy, it can be seen that the elongation of the alloy is obviously enhanced by hot extrusion deformation, which is consistent with the results of the mechanical properties test.

5. Conclusions

In this paper, the hot processing maps of A357 alloy were established in different deformation conditions, and optimum hot processing parameters were obtained by these hot processing maps and microstructure characteristics. The hot extrusion of A357 alloy was conducted according to the optimum parameters. The influence of hot extrusion on the mechanical properties was investigated. The conclusions can be summarized as follows:

(1) The instability deformation of A357 alloy mainly occurs in the high strain rate region (10 s^{-1}). With the increase in strain, the instability region expands to high temperature (470 °C).

(2) The ideal deformation conditions are temperatures of 380-410 °C and strain rates of 0.001-0.01 s^{-1}, and deformation temperatures of 440-470 °C and strain rates of 0.01-1 s^{-1} at the true strain of 0.5. When selected to deform under this deformation condition, the eutectic silicon is fine and uniform.

(3) A357 alloy is successfully extruded by hot extrusion with the optimal hot processing parameters. The mechanical properties of the as-extruded A357 alloy are improved compared with those of as-cast alloy, particularly when the elongation is up to 19.5%. In comparison with the original as-cast alloy, the fracture mechanism changes to ductile fracture.

Conflict of interest

The authors declare that they have no conflict of interest.

References

1. N.D. Alexopoulos and G. Pantelakis Sp, Quality Evaluation of A357 Cast Aluminum Alloy Specimens Subjected to Different Artificial Aging Treatment, *Mater. Des.*, 2004, **25**(5), p 419–430

2. O.S. Es-Said, D. Lee, W.D. Pfost, D.L. Thompson, M. Patterson, J. Foyos, and R. Marloth, Alternative Heat Treatments for A357-T6 Aluminum Alloy, *Eng. Fail. Anal.*, 2002, **9**(1), p 99–107

3. Z.W. Chen, P. Chen, and L. Fan, Effects of Melt Treatment on Dendrite Coherency of A357 Alloy, *Adv. Mater. Res.*, 2011, **189-193**, p 3886–3890

4. P.Y. Li, J. Jia, J.J. Guo, P.J. Li, and G.L. Shao, Effect of Melt Superheating on Microstructure and Mechanical Properties of A357 Alloy, *T. Nonferr. Metal Soc.*, 1997, **7**(3), p 94–98

5. M. Mostafaei, M. Ghobadi, G.B. Eisaabadi, M. Uludağ, and M. Tiryakioğlu, Evaluation of the Effects Of Rotary Degassing Processing Variables on the Quality of A357 Aluminum Alloy Castings, *Metall. Mater. Trans. B*, 2016, **47**(6), p 3469–3475

6. K.N. Prabhu and P. Hemanna, Heat Transfer During Quenching of Modified and Unmodified Gravity Die-Cast A357 Cylindrical Bars, *J. Mater. Eng. Perform.*, 2006, **15**(3), p 311–315

7. Y.Z. Zou, Z.B. Xu, and J.M. Zeng, Effects of Secondary Dendrite Arm Spacing on Microporosity of A357 Alloy, *Adv. Mater. Res.*, 2010, **97-101**, p 781–784

8. J.W. Yeh and W.P. Liu, Cracking Mechanisms of Silicon Particles in an A357 Aluminum Alloy, *Metall. Mater. Trans. A*, 1996, **27**(11), p 3558–3568

9. Y.C. Tzeng, V.S. Chengn, J.K. Nieh, H.Y. Bor, and S.L. Lee, Microstructure and Thermal Stability of A357 Alloy with and Without the Addition of Zr, *J. Mater. Eng. Perform.*, 2017, **26**(11), p 5511–5518

10. A. Saboori, M. Pavese, C. Badini, and A.R. Eivani, Studying the Age Hardening Kinetics of A357 Aluminum Alloys Through the Johnson-Mehl-Avrami Theory, *Met. Powder Rep.*, 2017, **72**(6), p 420–424

11. A. Bloyce and J.C. Summers, Static and Dynamic Properties of Squeeze-Cast A357-SiC Particulate Duralcan Metal Matrix Composite, *Mater. Sci. Eng., A*, 1991, **135**(1-2), p 231–236

12. S. Dezecot and M. Brochu, Microstructural Characterization and High Cycle Fatigue Behavior of Investment Cast A357 Aluminum Alloy, *Int. J. Fatigue*, 2015, **77**, p 154–159

13. W. Chen, Y.P. Guan, and Z.H. Wang, Hot Deformation Behavior of High Ti 6061 Al Alloy, *T Nonferr. Metal Soc.*, 2016, **26**(2), p 369–377

14. J. Peng, Y.J. Wang, L.P. Zhong, L.F. Peng, and F.S. Pan, Hot Deformation Behavior of Homogenized Al-32 Mg-04Er Aluminum Alloy, *T Nonferr. Metal. Soc.*, 2016, **26**(4), p 945–955

15. Q.G. Wang, Plastic Deformation Behavior of Aluminum Casting Alloys A356/357, *Metall. Mater. Trans. A Phys. Metall. Mater. Sci.*, 2004, **35A**(9), p 2707–2718

16. X.W. Yang, Z.H. Lai, J.C. Zhu, Y. Liu, and D. He, Hot Compressive Deformation Behavior of the As-Quenched A357 Aluminum Alloy, *Mater. Sci. Eng., B*, 2012, **177**(19), p 1721–1725

17. M. Haghshenas, A. Zareihanzaki, and M. Jahazi, An Investigation to the Effect of Deformation-Heat Treatment Cycle on the Eutectic Morphology and Mechanical Properties of a Thixocast A356 Alloy, *Mater. Charact.*, 2009, **60**(8), p 817–823

18. A. Abbasi-Bani, A. Zarei-Hanzaki, M.H. Pishbin, and N. Haghdadi, A Comparative Study on the Capability of Johnson-Cook and Arrhenius-Type Constitutive Equations to Describe the Flow Behavior of Mg-6Al-1Zn Alloy, *Mech. Mater.*, 2014, **71**, p 52–61

19. A. Yanagida and J. Yanagimoto, A Novel Approach to Determine the Kinetics for Dynamic Recrystallization by Using the Flow Curve, *J. Mater. Process. Tech.*, 2004, **151**(1-3), p 33–38

20. Y. Prasad and S. Sasidhara, *Hot Working Guide: A Compendium of Processing Maps*, ASM International, Materials Park, 1997, p 25–177

21. Y. Prasad, H.L. Gegel, and S.M. Doraivelu, Modeling of Dynamic Material Behavior in Hot Deformation: Forging of Ti-6242, *Metall. Trans. A*, 1984, **15**(10), p 1883–1892

22. H. Mirzadeh, A. Najafizadeh, and M. Moazeny, Flow Curve Analysis of 17-4 PH Stainless Steel Under Hot Compression Test, *Metall. Mater. Trans. A*, 2009, **40**(12), p 2950–2958

23. T.K. Ha, W.J. Park, S.G. Ahn, and Y.W. Chang, Fabrication of Spray-Formed Hypereutectic Al-25Si Alloy and its Deformation Behavior, *J. Mater. Process. Tech.*, 2002, **130**, p 691–695

24. H.Z. Wang, K. Zhang, X.G. Li, and Y.J. Li, Effects of Homogenization on Hot Deformation Behaviors of AZ80 Magnesium Alloys with Processing Map, *T. Nonferr. Metal Soc.*, 2010, **20**(9), p 1671–1679

25. H.Z. Zhao, L. Xiao, P. Ge, J. Sun, and Z.P. Xi, Hot Deformation Behavior and Processing Maps of Ti-1300 Alloy, *Mater. Sci. Eng., A*, 2014, **604**, p 111–116

26. J.Z. Xu, X.J. Gao, Z.Y. Jiang, and D.B. Wei, A Comparison of Hot Deformation Behavior of High-Cr-White Cast Iron and High-Cr White Cast Iron/Low Carbon Steel Laminate, *Steel Res. Int.*, 2016, **87**(6), p 780–788

27. F.W. Kang, J.F. Sun, G.Q. Zhang, Z. Li, and J. Shen, Characteristics of Hot Compression Deformation and Microstructure Evolution of Spray Formed Nickel Base Superalloy, *Acta. Metall. Sinica.*, 2007, **43**(10), p 1053–1058

28. X. Yang and W. Li, Flow Behavior and Processing Maps of A Low-Carbon Steel During Hot Deformation[J], *Metall. Mater. Trans. A*, 2015, **46**(12), p 6052–6064

29. B.L. Xiao, J.Z. Fan, and X.F. Tian, Hot deformation and processing map of 15%SiCp/2009 Al composite, *J. Mater. Sci.*, 2005, **40**, p 5757–5762

30. B.L. Xiao, J.Z. Fan, X.F. Tian et al., Hot Deformation and Processing Map of 15% SiC p/2009 Al Composite, *J. Mater. Sci.*, 2005, **40**(21), p 5757–5762

31. R.K.W. Marceau, G. Sha, and R.N. Lumley, Evolution of Solute Clustering in Al-Cu-Mg Alloys During Secondary Ageing, *Acta Mater.*, 2010, **58**(5), p 1795–1805

32. N. Chobaut, D. Carron, and J.M. Drezet, Characterisation of Precipitation Upon Cooling of an AA2618 Al-Cu-Mg Alloy, *J. Alloys Compd.*, 2016, **654**, p 56–62

33. Y. Prasad and T. Seshacharyulu, Modelling of hot deformation for microstructural control, *Int. Meter. Rev.*, 1998, **43**(6), p 243–258

34. G. Ganesan, K. Raghukandan, and R. Karthikeyan, Development of Processing Maps for 6061 Al/15% SiCp Composite Material, *Mater. Sci. Eng., A*, 2014, **369**(1), p 230–235

35. S. Banerjee, P.S. Robi, and A. Srinivasan, Deformation Processing Maps for Control of Microstructure in Al-Cu-Mg Alloys Microalloyed with Sn, *Metall. Mater. Trans. A*, 2012, **43**(10), p 3834–3849

36. A.K. Maheshwari, Prediction of flow Stress for Hot Deformation Processing, *Comp. Mater. Sci.*, 2013, **69**, p 350–358

37. M. Haghshenas, A. Zarei-Hanzaki, S.M. Fatemi-Varzaneh, and H. Abedi, Hot Deformation Behaviour of Thixocast A356 Aluminum Alloy During Compression at Elevated Temperature, *Int. J. Mater. Form.*, 2008, **1**(1), p 1001–1005